Nano Research

Open Access

Research Article

Mesoporous N-incorporated carbon with Ti single atom-regulated electronic structure as high performance cathodes for Li-S batteries

Jiafeng Hu[1,§], Yunfei Xiao[2,§], Zhengguang Hu[1,§], Guanghao He[1], Zhongheng Zhu[1], Fengping Xie[1], Li Wang[1], Li Zuo[2], and Yong Zhao[1] ✉

[1] Department of Physics, School of Physics and Materials Science, Nanchang University, Nanchang 330031, China
[2] National Engineering Research Center for Bioengineering Drugs and the Technologies, Institute of Translational Medicine, Jiangxi Medical College, Nanchang University, Nanchang 330031, China
§ Jiafeng Hu, Yunfei Xiao, and Zhengguang Hu contributed equally to this work.

Cite this article: *Nano Research*, **2025**, *18*, 94907114. https://doi.org/10.26599/NR.2025.94907114

ABSTRACT: Lithium-sulfur (Li-S) batteries are considered as strong competitors for next-generation energy storage because of their high theoretical energy density. However, some challenges, such as shuttle effect of lithium polysulfides (LiPSs), volume expansion of sulfur during charge/discharge process and poor conductivity of the cathode, hindered their commercial application. In this paper, an excellent sulfur host material, the titanium single atom (TiSA)-anchored mesoporous N-incorporated carbon (TiSA-NC) was successfully obtained. The introduction of TiSAs onto the NC textures optimized their electronic structures including the charge distribution between the constituent atoms and the total density of states (TDOS) near the Fermi level. Consequently, the button battery constructed by TiSA-NC delivered impressive energy storage performance: a high reversible capacity of 1077 mAh·g^{-1} at 0.1 C; an outstanding rate capacity of 541 mAh·g^{-1} at 3 C; a superior long-term stability with a capacity fading rate of 0.053% per cycle for 500 cycles at 0.5 C. This work provided an effective strategy for manufacturing high performance Li-S batteries by designing and constructing single atom catalysts.

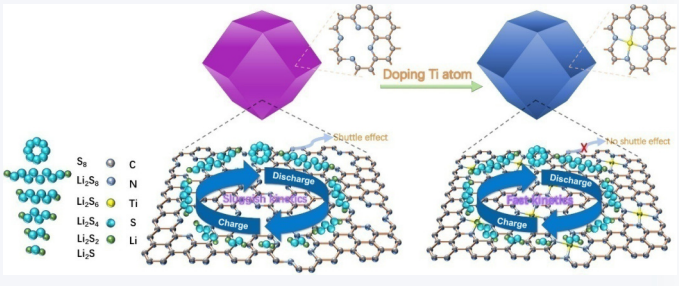

KEYWORDS: lithium-sulfur (Li-S) battery, single atoms, electronic structure, catalyst, kinetics

1 Introduction

Lithium-sulfur (Li-S) batteries are appealing for their high theoretical energy density (2600 Wh·kg^{-1}) and specific capacity (1675 mAh·g^{-1}), with resource-abundant and environmentally friendly sulfur element as the active cathode [1–3]. However, there are still many drawbacks that hinder the development of the Li-S batteries, such as the shuttle effect, poor conductivity of the cathode and drastic volume changes of the electrodes. The shuttle effect is that the polysulfide migrates back and forth between the cathode and anode, which will cause irreversible loss of the active materials and poison the cycle performance [4–6]. The poor electrical/ionic conductivity of the cathode aroused from the insulativity of the sulfur/Li_2S_2/Li_2S species, resulting in the increasement of the internal resistance hence the slackness in redox kinetics and the reducement of the utilization of the active materials [7]. On cycling, the maximal volume expansion of sulfur is close to 80%, which will mechanically hurt the structure of the battery and deteriorate its stability and safety [8, 9].

High efficiency cathodic catalyst plays a key role in relieving the above-mentioned drawbacks of the Li-S batteries. In recent years, exploitation has been paid for designing and constructing optimum sulfur host incorporated with effective redox electrocatalyst and great progress has been made [10–12]. Among all the sulfur host candidates, porous carbonaceous materials [13], which feature vast specific surface area and high electrical conductivity, have been considered promising, as they can accommodate and physically confine the sulfur species by ubiquitous pores and electrically accelerate the redox kinetics. However, due to non-polarity of the carbonaceous materials, they cannot chemically limit the shuttle effect of the polar lithium polysulfides (LiPSs) and the weak

Received: August 30, 2024; **Revised:** October 21, 2024
Accepted: November 4, 2024

✉Address correspondence to zhaoyong@ncu.edu.cn

connection between the host and the LiPSs is disadvantageous for electron transport and hence the sluggish redox kinetics [14]. Introducing heterogeneous atoms or groups onto the surface of the carbonaceous materials, which is favourable for polarity enhancement and electronic structure adjustment, is an effective way to further chemically improve the restriction strength and the redox kinetics in reversible conversion process of the LiPSs [15, 16].

Single-atom catalysts (SACs), with isolated metal atoms monodispersing on various solid two-dimensional substrates, have attracted wide attention in recent years [17]. Theoretically they can achieve 100% atomic utilization and thus have a much higher activity than conventional metal nanoparticle catalysts [18]. Various SACs have been explored for enhancing the electrochemical performance of Li-S batteries. Liu's group used Fe SACs anchored on nitrogen-rich metal organic frameworks (MOF) derived carbon nanocage serving as bifunctional catalysts to facilitate both the decomposition and the formation of Li_2S [19]. Li's group dispersed Co atoms on hierarchical carbon nitride (C_3N_4) support to exert efficient catalytic effects on LiPSs [20]. Chen et al. prepared Ni atoms on nitrogen-doped graphene (Ni@NG) to modify the separators which can both chemically trap LiPSs and accelerate redox kinetics [21]. Under the guidance of density functional theory (DFT) calculations, Cui et al. successfully designed V SACs inserted on graphene toward fast kinetic and long-life Li-S batteries [22]. More recently, Cheng's group used d–p orbital hybridization to elucidate the catalytic mechanism of SACs in Li-S batteries and researched a series of SACs (SATi, SAMn, SACr, SACu) embedded in three-dimensional (3D) carbon foams for verification, the SATi has the highest catalytic activity, the results show that the SATi exhibits the highest catalytic activity, which matching well with the calculations [23]. SACs associated with carbonaceous materials typically adopt square-planar M-N_4 model with each metal atom anchored by tetradic nitrogen atoms. The introduction of an isolated metal atom onto one lattice site of the carbonaceous materials would optimize the charge distribution and adjust electronic conductivity, which affords an effective tactic to boost the electrochemical performance of the Li-S batteries through defect engineering [24, 25].

Herein, the titanium single atom-anchored mesoporous N-incorporated carbon (TiSA-NC) which was prepared by pyrolysis of titanium incorporated zeolitic imidazolate framework-8 (Ti-ZIF-8) was adopted as sulfur host for Li-S batteries. The synthesis process of Ti-ZIF-8 was similar to the conventional ZIF-8 precursor, except for a small amount of titanium acetyl acetone was added in the zinc nitrate solution [26, 27]. The TiSA-NC inherited the large surface area and affluent porous structure from Ti-ZIF-8 which were prerequisite for abundant active sites, shortened transportation paths for electrons and lithium ions. Furthermore, the introduction of an isolated Ti atom onto one lattice site of NC adjusted the density of states (DOS) at the Fermi level and optimized the charge distribution between the constituent atoms, thus the improved electronic conductivity, the strengthened polarity and hence the enhanced adsorption energies (E_{ads}) toward LiPSs, consequently ensured that LiPSs convert reversibly with accelerated electron transportation, declined reaction barrier in the rate-limiting step and inhibition on shuttle effect, which are conducive for enhancing the performance of the Li-S batteries. Therefore, electrochemical performance and cycling stability delivered by the Li-S batteries based on the TiSA-NC was better than that based on NC, including a specific capacity of 1077 mAh·g^{-1} at 0.1 C, a rate performance of 541 mAh·g^{-1} at 3 C and an average decay rate of 0.053% per cycle at 0.5 C for 500 cycles.

2 Experimental

2.1 Materials

2.1.1 *Synthesis of Ti-ZIF-8 and ZIF-8*

Dimethylimidazole (1.31 g, 16 mmol) was dissolved in 15 mL methanol to get solution A. Titanium acetyl acetone (0.05 g, 0.2 mmol) and zinc nitrate hexahydrate (1.19 g, 4 mmol) were dissolved in 30 mL methanol to obtain solution B. The solution A and B were treated by ultrasonic dispersion for 15 min to obtain the transparent solution. Solution B was rapidly added to solution A for another 15 min stirring and the mixture which had been let stand for 12 h at room temperature was separated into two layers with a transparent solution on the upper and a white precipitate on the bottom. After the precipitate was purified by centrifugation (10,000 rpm, 7 min), rinsing once with N,N-dimethylformamide (DMF) and thrice with methanol and then drying overnight under vacuum at 60 °C, the final product Ti-ZIF-8 was obtained. ZIF-8 was synthesized by the same method except that titanium acetyl acetone was excluded from the precursors.

2.1.2 *Synthesis of TiSA-NC and NC*

The TiSA-NC was obtained by the pyrolysis of Ti-ZIF-8. The pyrolysis procedure was fulfilled by annealing Ti-ZIF-8 under an argon flow at 900 °C for 2 h, with the heating rate of 5 °C·min^{-1}, then cooling to room temperature in Ar atmosphere. NC was obtained by the similar pyrolysis procedure for the synthesis of TiSA-NC except that Ti-ZIF-8 was substituted by ZIF-8.

2.1.3 *Synthesis of TiSA-NC/S and NC/S*

The obtained TiSA-NC or NC was evenly mixed with sulfur powder at a mass ratio of 7:3 and heated at 155 °C for 6 h. After the sample was cooled to room temperature, TiSA-NC/S or NC/S was obtained.

2.1.4 *Synthesis of Li_2S_6 solution*

The Li_2S_6 solution was fabricated by mixing sulfur powder and Li_2S powder (1:5 moles) in a mixed solution of 1,2-dimethoxyethane (DME) and 1,3-dioxolane (DOL, volume ratio V:V = 1:1) then keeping stirred at 70 °C for 24 h.

2.2 Assembly of symmetric cells

The symmetric cells were assembled by two identical TiSA-NC or NC electrodes with an electrolyte containing 0.42 M Li_2S_6 additive and a piece of Celgard 2400 as the separator. The electrolyte was a solution with 1.0 M lithium bis(trifluoromethanesulphonyl)imide (LiTFSI) and 2% lithium nitrate dissolved in a mixture of 1,3-dioxolane and 1,2-dimethoxyethane (V:V = 1:1). The cyclic voltammetry (CV) curves of symmetric cells were tested at a scan rate of 1 mV·s^{-1} in a range from −1.0 to 1.0 V.

2.3 Polysulfide adsorption test

To survey the adsorption affinity of the materials, NC and TiSA-

NC with identical weight were separately added into two bottles of 5 mM Li_2S_6 solution with equal volume and another bottle of 5 mM Li_2S_6 solution was selected as comparison. The samples were let stand for 10 h in a glove box filled with argon gas to fulfill the test.

2.4 Nucleation of Li_2S

To obtain the electrolyte containing 0.5 M Li_2S_8, sulfur powder and Li_2S powder (molar ratio of 7:1) are mixed in the electrolyte mentioned in the above Section 2.2 for a 24 h stirring at 50 °C. The 2025 coin battery (CR2025) was assembled by adopting TiSA-NC or NC as the cathode, with a slice of Li foil as the anode and a piece of Celgard 2400 as the separator, which was soaked with the electrolyte containing 0.5 M Li_2S_8. The assembled battery was discharged to 2.06 V with a constant current of 0.110 mA and then potentiostatically discharged at 2.05 V for 2000 s.

2.5 Materials characterizations

The microstructure and morphology of NC and TiSA-NC were characterized using cold field emission scanning electron microscopy (SEM, ZEISS Sigma300, 3 kV) and transmission electron microscopy (TEM, JEOL JEM 2100, 200 kV). The high-angle annular dark-field scanning TEM (HAADF-STEM) was taken by JEM-ARM200F NEOARM. Raman spectra were performed by Thermo Scientific DXR. X-ray diffraction (XRD) spectra was carried out with a D8 ADVANCE. X-ray photoelectron spectroscopy (XPS) measurements were performed on ESCALAB250Xi. Thermogravimetric analysis (TGA) was measured from room temperature to 500 °C in argon, on a STA PT 1600 thermogravimetric analyzer. The specific surface area and the pore diameter distribution were collected on a JW-BK 132F instrument.

2.6 Electrochemical measurement

70 wt.% TiSA-NC/S (or NC/S), 20 wt.% carbon black, 10 wt.% polyvinylidene fluoride (PVDF) were mixed in N-methylpyrrolidinone (NMP) to get a uniform slurry by stirring. The slurry was coated on the aluminum foil and then dried in a vacuum drying oven at 60 °C for 12 h. CR2025 were assembled with lithium foil anode, TiSA-NC/S or NC/S composite cathode and Celgard 2400 separator. The sulfur loading of the cathode was between 1.0 and 1.7 mg·cm^{-2}. The corresponding electrolyte volume/sulfur mass (E/S) ratio was 30 μL·mg^{-1}. The galvanostatic charge–discharge tests were carried out in the potential range of 1.7–2.8 V through the Neware battery test devices. CV cycling curves (0.1–0.5 mV·s^{-1}) and electrochemical impedance spectroscopy (EIS) spectra (10^{-1}–10^5 Hz, 5 mV) were analyzed with the help of a CorrTest CS350H Electrochemical Workstation.

2.7 DFT calculations

All calculations were performed by using the projector augmented wave method in the framework of DFT, as implemented in the Vienna *ab initio* simulation package (VASP) [28]. The electron exchange-correlation interactions were parameterized by the generalized gradient approximation (GGA) with the Perdew–Burke–Ernzerhof (PBE) [29, 30]. Spin polarization effect was considered in this work. The plane-wave energy cutoff was set to 500 eV and the convergence tolerance for residual force and energy on each atom during structure relaxation were set to 0.02 eV·Å^{-1} and 10^{-5} eV, respectively. The Brillouin zone was sampled by Gamma-centered k-point with 2 × 2 × 1 mesh scheme for structural relaxation and 6 × 6 × 1 for the calculation of the DOS. The dispersion correction D3 was included in the DFT calculation by using the zero damping approach [31]. To prevent the interaction between two adjacent periodic images, a 20 Å vacuum layers were set along the z-axis. Structural and electric density visualization was conducted utilizing the visualization for electronic and structural analysis (VESTA) software [32]. The VASPKIT code is used to finish the pre- and post-processing of the calculation results [33]. The climbing-image nudged elastic band (CI-NEB) method, as implemented in VASP, was used to investigate transition states, which were then characterized by frequency analysis to ensure a single imaginary frequency in the desired reaction direction [34].

3 Results and discussion

The synthesis process of TiSA-NC was shown in Fig. 1(a). The Ti-ZIF-8 was acquired by adding dimethylimidazole, titanium acetyl acetone and zinc nitrate hexahydrate to methanol and then letting stand for 12 h at room temperature. By adopting Ti-ZIF-8 as precursor, TiSA-NC was obtained through pyrolyzing the precursor at 900 °C in argon. Then, sulfur was infiltrated into TiSA-NC by melt-diffusion method to assemble TiSA-NC/S. SEM images in Figs. 1(b) and 1(c) showed that the TiSA-NC had dodecahedral morphology at different magnifications and the structure of TiSA-NC did not change significantly compared with NC (Fig. S1 in the Electronic Supplementary Material (ESM)). The dodecahedron structure of TiSA-NC could also be observed by TEM (Figs. 1(d) and 1(e)) and there was no evidence of nanoparticles aggregation on the surface of TiSA-NC [35]. The energy dispersive spectrum (EDS) element mapping images showed that C, N and Ti elements were uniformly distributed in TiSA-NC (Fig. 1(g)). The existence form of Ti atoms was observed by aberration-corrected HAADF-STEM image. As shown in Fig. 1(f), it could be clearly observed that many bright dots scattered over support corresponded to TiSAs.

The chemical and electronical structure of TiSA-NC was analyzed by XRD, Raman spectra and XPS. The XRD pattern of TiSA-NC in Fig. 2(a) showed that two typical peaks of carbon near 22° and 44°, corresponding to the (002) and (100) crystal planes of carbon, respectively, without any Ti crystallization peaks were detected, which indicated that no Ti nanoparticles or clusters were formed. The Raman spectra of two samples showed that the I_D/I_G (this is the intensity ratio of the disordered carbon (D-band) and the graphitic carbon (G-band)) of NC and TiSA-NC were 1.07 and 1.18, as shown in Fig. 2(b), indicating that the introduction of TiSAs enhanced the defect density of the material. The N 1s XPS spectra of TiSA-NC given in the Fig. 2(c) showed that four characteristic peaks at 398.6, 399.2, 400.3 and 401.5 eV correspond to pyridinic N, Ti–N, pyrrolic N and graphitic N, respectively. Obviously, pyridinic N was the dominant N species, which were favourable for promoting electron transfer process [36]. The peak corresponding to Ti–N coordination was present in the N 1s XPS spectrum of TiSA-NC (Fig. 2(c)) while absent in that of NC (Fig. 2(d)). In addition, the Ti 2p XPS spectra of TiSA-NC in Fig. S2 in the ESM showed that there were Ti $2p_{1/2}$ and $2p_{3/2}$ peaks at 463.0 and 457.6 eV, respectively, which were attributed to Ti–N binding [32]. The pore size and specific surface area of NC and TiSA-NC were obtained by nitrogen adsorption–desorption isotherms. The results (Figs. 2(e) and 2(f)) showed that the specific surface area of NC and TiSA-NC were 805.691 and 709 m^2·g^{-1} and the corresponding average pore sizes were 7.779 and 5.641 nm. The smaller specific surface area of TiSA-NC compared with NC may

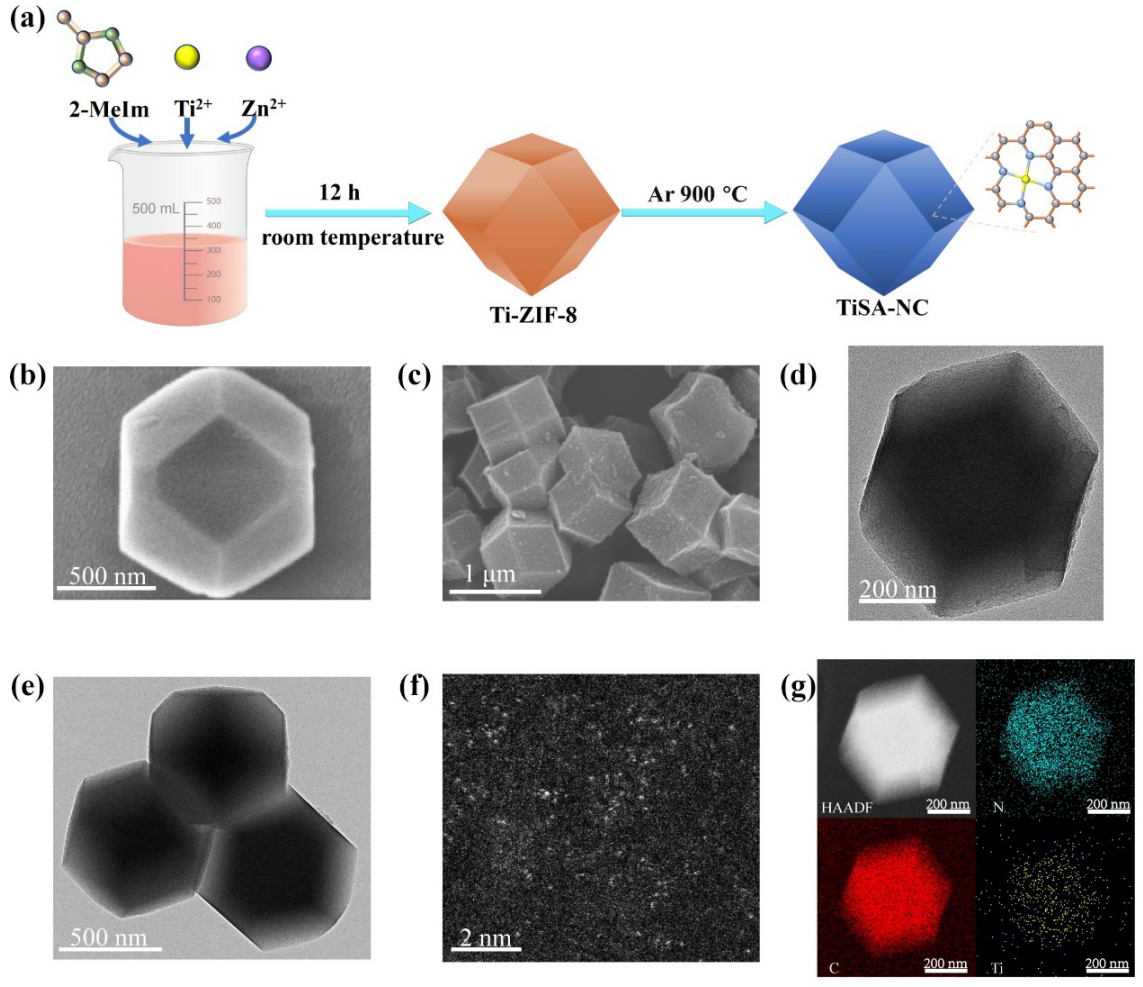

Figure 1 Synthesis and morphology characterization of TiSA-NC. (a) Schematic illusion of synthesis procedures. (b) and (c) SEM images of TiSA-NC material at different magnifications. (d) and (e) TEM images of TiSA-NC material at different magnifications. (f) HAADF-STEM image of TiSA-NC. (g) HAADF image and corresponding EDS mappings of TiSA-NC.

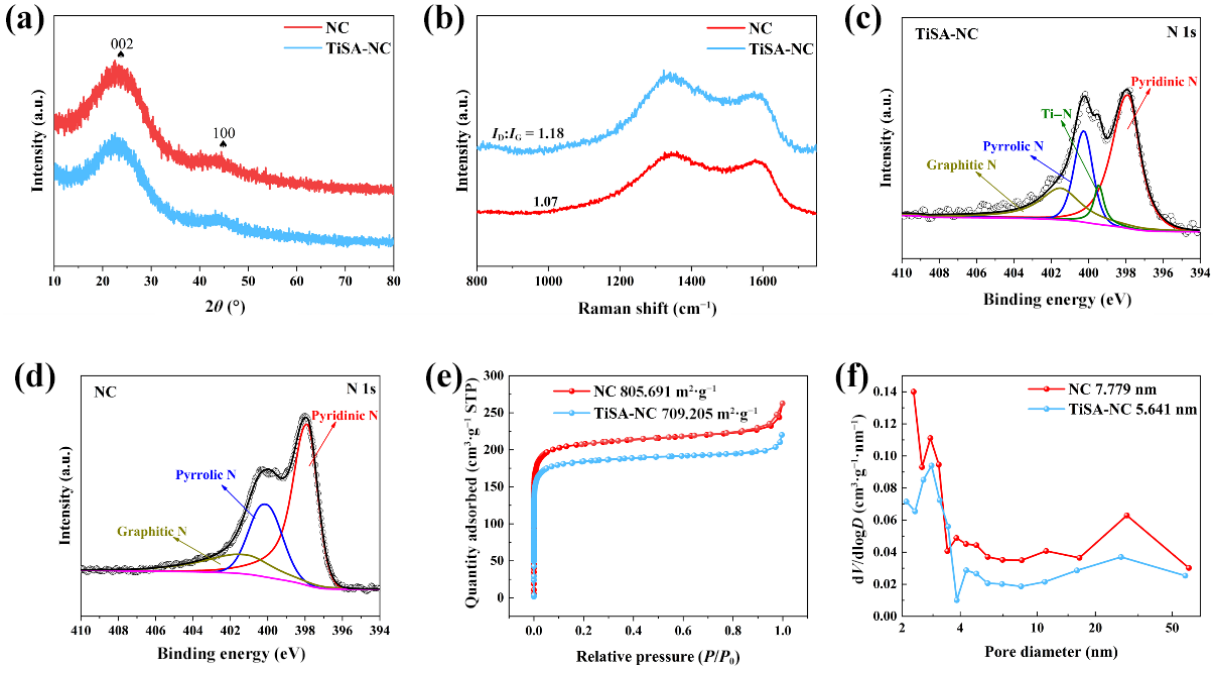

Figure 2 Chemical structure analysis of TiSA-NC and NC. (a) XRD patterns of NC and TiSA-NC materials. (b) Raman spectra of NC and TiSA-NC. N 1s XPS spectra of (c) TiSA-NC and (d) NC. (e) Nitrogen adsorption–desorption isotherms and (f) corresponding distribution of pore size in TiSA-NC and NC.

be due to the introduction of Ti atoms diluted specific surface area value [33]. The large specific surface area and abundant mesoporous in the synthesized TiSA-NC could provide sufficient reaction interface with abundant active sites and shortened transport paths for electrons and lithium ions. The XRD patterns (Fig. S3 in the ESM) of TiSA-NC/S and NC/S showed similar diffraction peaks in accordance with sulfur (PDF #99-0100), indicating that the sulfur was successfully infiltrated into NC and TiSA-NC. The TGA showed that the sulfur content of TiSA-NC/S (Fig. S4 in the ESM) and NC/S (Fig. S5 in the ESM) was 72.414 wt.%, 70.4309 wt.%, respectively. The sulfur content of the two materials were almost equal, which showed that the introduction of TiSAs did not affect the sulfur loading significantly [34].

In order to explore the adsorption capability of TiSA-NC for polysulfide, TiSA-NC was dissolved in 5 mM Li_2S_6 solution and left static for 10 h for polysulfide adsorption test. The Li_2S_6 solution with TiSA-NC was almost colorless after 10 h, whereas the solution with NC showed only a slight color change, as shown in Fig. 3(a). The obvious color change indicated that TiSA-NC had stronger adsorption capability for Li_2S_6 than NC. The electrocatalytic effect of TiSA-NC on polysulfide conversion was further investigated by symmetric cells. As shown in Fig. 3(b), at a scanning rate of 1 mV·s^{-1}, TiSA-NC had a higher current response and larger peak area than NC, indicating that TiSA-NC had a great promotion effect on the redox conversion rate of polysulfide. The CV was adopted to survey the electrocatalytic ability of TiSA-NC and NC coin cells. CV curves (Fig. 3(c)) showed that both TiSA-NC and NC had an anodic geminal peak (peak 1) and two cathodic peaks (peak 2 & 3). The subpeak at lower potential in Peak 1 reflected the transformation of Li_2S into Li_2S_x ($4 \le x \le 8$), while the subpeak at higher potential reflected the formation of S_8. Peaks 2 and 3 corresponded to the conversion of S_8 to Li_2S_x and then to Li_2S, respectively. Cell based on TiSA-NC had a higher peak current than that based on NC, with the corresponding cathodic peaks shifted positively and anodic peaks shifted negatively, demonstrating that the former had a stronger catalytic effect on reversible conversion of LiPSs with a more lowered polarization and a faster redox kinetics. The diffusion efficiency of lithium ions (D_{Li^+}) was one of the indexes for quantifying the catalytic kinetics of LiPSs redox reactions. CV measurements were used to examine the D_{Li^+}. The scan-rate-dependent CV curves of the cells based on TiSA-NC and NC were displayed in Figs. 3(d) and 3(e), respectively, which were conducted in the 1.7–2.8 V region with a scan rate ranging from 0.1 to 0.5 mV·s^{-1}. According the Randles Sevick equation, the slope of the fitted line between the CV peak currents and the square root of the scanning rates can be considered as D_{Li^+}, as which is proportionally related with the D_{Li^+} [35, 36]. The slope values corresponding to the peaks 1–3 of the cells based on TiSA-NC/S were significantly higher than those based on NC/S (Fig. 3(f)),

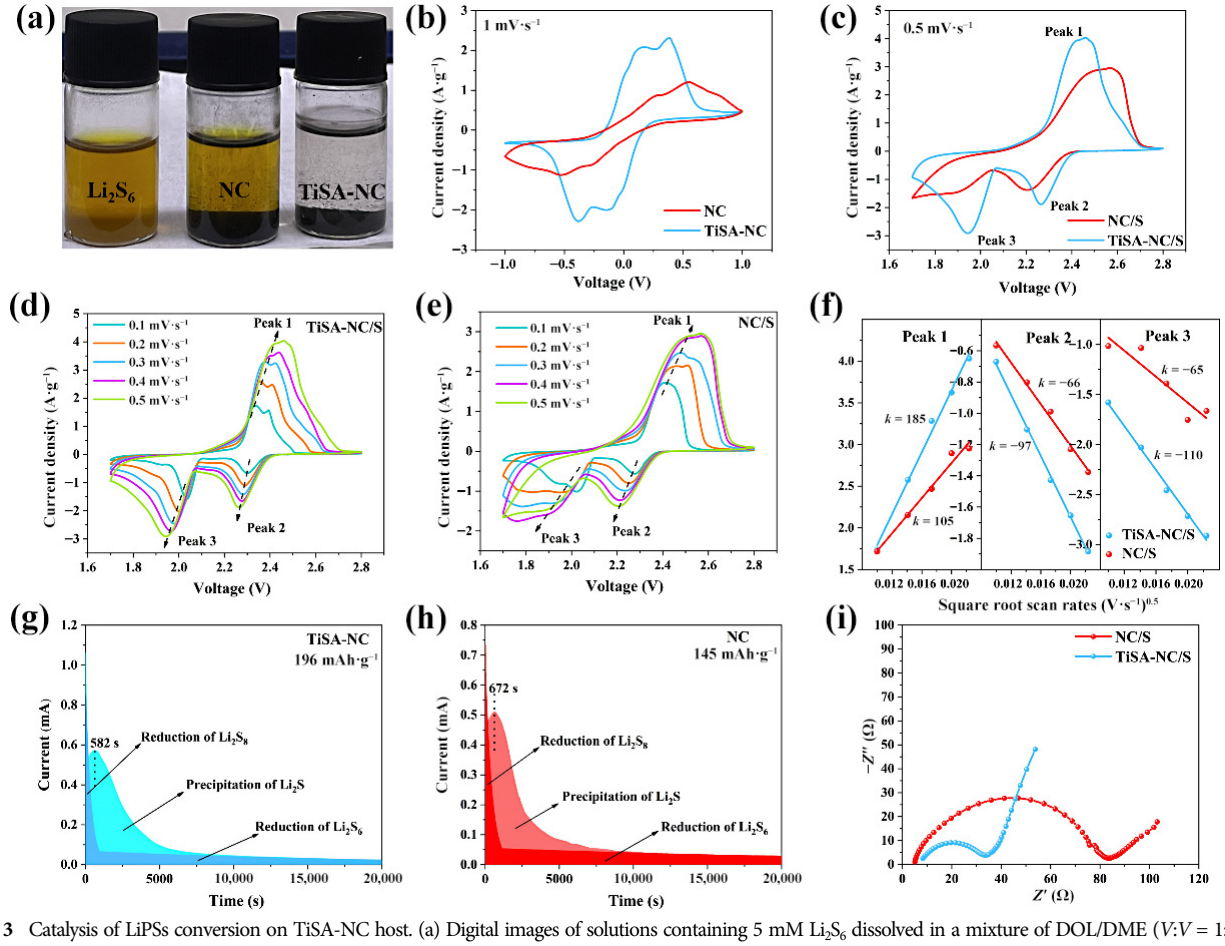

Figure 3 Catalysis of LiPSs conversion on TiSA-NC host. (a) Digital images of solutions containing 5 mM Li_2S_6 dissolved in a mixture of DOL/DME (V:V = 1:1) after contacting with TiSA-NC and NC for 24 h. (b) CV curves of Li_2S_6 symmetric cells with the NC and TiSA-NC electrode at 1 mV·s^{-1}. (c) CV profiles of NC/S and TiSA-NC/S electrode at the scan rate of 0.5 mV·s^{-1}. CV curves of (d) Ti-NC/S and (e) NC/S electrode under various scan rates. (f) Plots of the peak currents versus square root of scan rates. Li_2S deposition profiles of (g) TiSA-NC/S and (h) NC/S electrode. (i) EIS diagrams of TiSA-NC/S and NC/S electrode at 0.1 C after 50 cycles.

which indicated the former had the higher D_{Li^+} favourable for promoting the polysulfide conversion kinetics. The huge specific surface area and abundant mesopores of the obtained carbonaceous material conferred a fast Li^+ transport [37], which was further boost by the incorporation of Ti atoms onto the NC texture. The polysulfide conversion efficiency was further explored by potentiostatic discharging test to motivate full reduction of Li_2S_8 to insoluble Li_2S in Li-S batteries based on TiSA-NC or NC. As shown in Figs. 3(g) and 3(h), the TiSA-NC afforded a quantity of Li_2S precipitation (196 mAh·g^{-1}) with a current peak at 582 s, which was larger than those afforded by NC (145 mAh·g^{-1}, 672 s). EIS is an important parameter reflecting battery redox kinetics. The batteries based on TiSA-NC displayed lower charge transfer resistance (R_{ct}) values (41.3 Ω) compared with NC (106.9 Ω) before cycling (Fig. S6 in the ESM). The R_{ct} was getting lower after 50 cycles (Fig. 3(i)), which should be attributed to the redispersion of LiPSs and the appearance of toxic LiPSs shutting [38].

Figure 4(a) showed the galvanostatic charge/discharge curves of NC/S and TiSA-NC/S electrode at 0.1 C. The TiSA-NC/S electrode had lower overpotential and higher discharge capacity than the NC/S electrode. The role of TiSA-NC in promoting polysulfide conversion was further studied by analyzing the rate performance of Li-S batteries. As shown in Fig. 4(b), the specific discharge capacity of NC/S electrode was 821, 665, 539, 378, 116, 30 mAh·g^{-1} at rate of 0.1, 0.2, 0.5, 1, 2 and 3 C and there was almost no capacity at 3 C. However, the specific discharge capacity of TiSA-NC/S electrode at 0.1, 0.2, 0.5, 1, 2 and 3 C was 1077, 919, 810, 726, 635 and 541 mAh·g^{-1}. In addition, when the current density gradually decreased from 3 to 1 and 0.5 C, TiSA-NC/S electrode recovered to the discharge capacity of the 713 and 819 mAh·g^{-1}, respectively, which indicating that the batteries with TiSA-NC/S electrode had better reversibility. The charge/discharge curves of NC/S and TiSA-NC/S electrode at the current densities ranging from 0.1 to 3 C corresponded to Figs. 4(c) and 4(d), respectively. It could be clearly discerned in Fig. 4(d) that TiSA-NC/S electrode maintained flat charge/discharge plateau at different rates, even at 3 C. Comparatively, the charge/discharge plateaus of the NC/S electrodes just about disappeared at high rates and the capacity shrunk dramatically with the increase of the rates, which was due to the deteriorated redox kinetics of polysulfide at high rates. The cyclability test of Ti-NC/S and NC/S electrode were operated at 1 C. Cycling of the batteries began with the activation procedure of charging/discharging for one round at 0.05 C, five round at 0.1 C and five round at 0.5 C, sequentially. As shown in Fig. 4(e), TiSA-NC/S electrode exhibit good cycling stability with nearly 100% Coulombic efficiency and a specific capacity of 532 mAh·g^{-1} after 200 cycles, while NC electrode had a final specific capacity of only 282 mAh·g^{-1}. Compared with the TiSA-NC/S cathode before cycling (Fig. S7 in the ESM), the surface morphology of the TiSA-NC/S cathode after cycling (Fig. S8 in the ESM) was well maintained and there was no obvious cumulated sulfur arose in TiSA-NC/S cathode, which indicated that the TiSA-NC catalysts could ensure the homogeneous deposition of sulfur in cathode. The long-term cyclability test was conducted at 0.5 C and the results were shown in Fig. 4(f). It exhibited that the TiSA-NC/S electrode maintained a capacity of 567 mAh·g^{-1} with an average decay rate of 0.053% per cycle after 500 cycles, while the NC/S electrode had a capacity of only 258 mAh·g^{-1} with an average decay rate of 0.070% per cycle. The Ti-NC/S electrode still exhibited excellent electrochemical performance compared to many reported S cathodes (Table S1 in the ESM) [37–41].

DFT calculations were employed to further elucidate the TiSAs-tailored electronic structures of NC textures and thus their electrocatalytic performance in Li-S batteries. The structural model of NC was presented in Fig. 5(a). According to the previous research and our XPS results [23], the most possible atomic arrangement of TiSA-NC is the typical square-planar M-N_4 model with M, the TiSA as the coordination center, as displayed in Fig. 5(b). The dissociation energy curves of Li_2S on NC and TiSA-NC were presented in Figs. 5(c) and 5(d), respectively. The latter is favourable for facile decomposition of Li_2S with an energy barrier of 0.9795 eV, which is much lower than the value on the former,

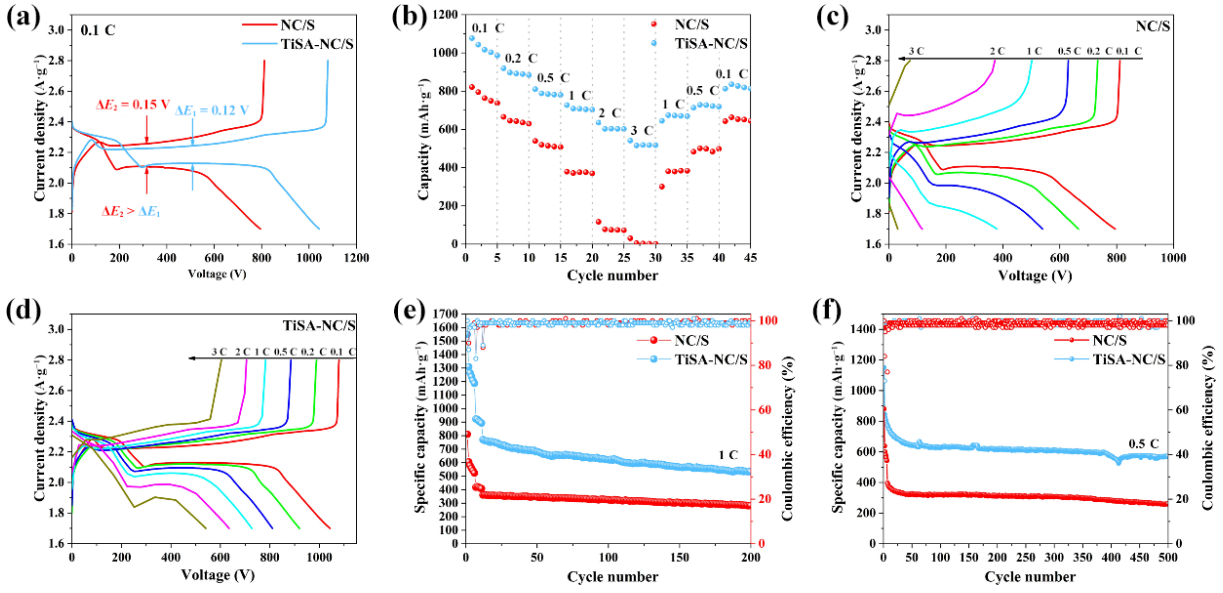

Figure 4 Electrochemical performance of Li-S batteries with TiSA-NC/S electrodes. (a) The charge/discharge curves of TiSA-NC/S and NC/S electrodes recorded at 0.1 C. (b) The rate performance of TiSA-NC/S and NC/S electrodes. Charge/discharge voltage profiles of (c) NC/S and (d) TiSA-NC/S electrodes at current rates of 0.1, 0.2, 0.5, 1.0, 2.0 and 3.0 C. (e) Cycling performance and Coulombic efficiency of the TiSA-NC/S and NC/S electrodes at 1 C for 200 cycles. (f) Long-term cycling stability of the TiSA-NC/S and NC/S electrodes at 0.5 C for 500 cycles.

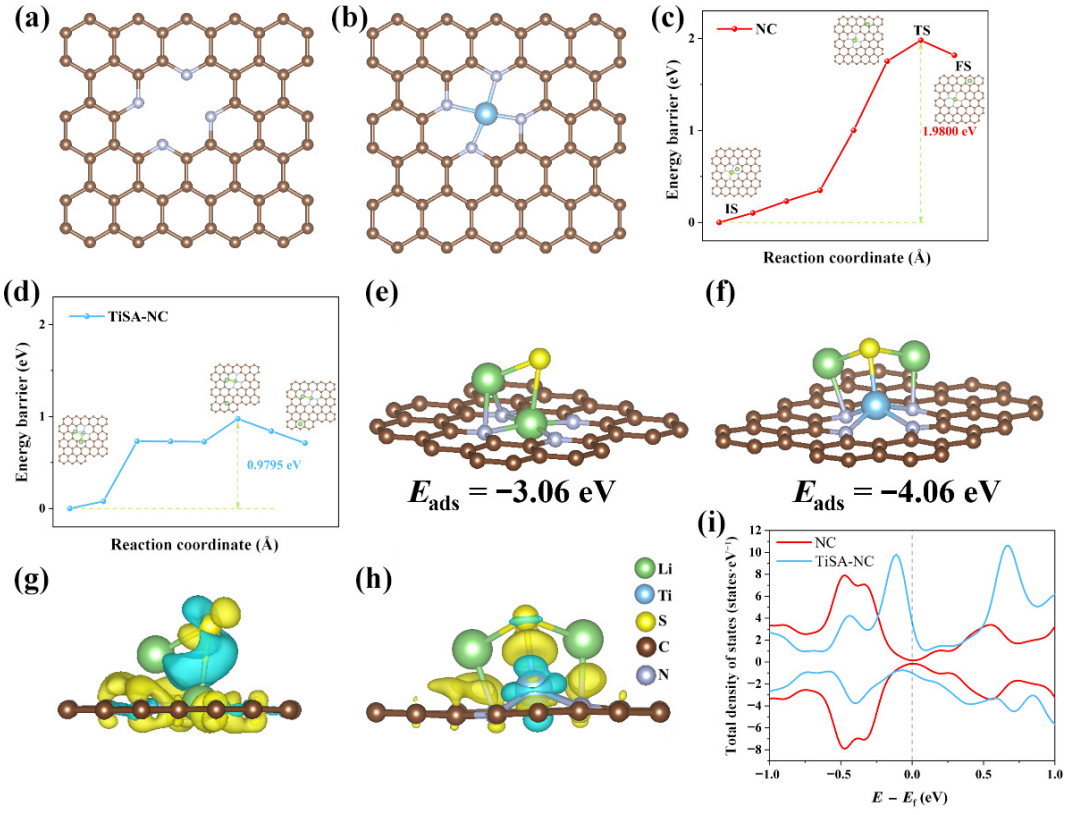

Figure 5 DFT calculations of the absorption structure of TiSA-NC and NC with Li_2S. Structural models of (a) NC and (b) TiSA-NC. The energy barrier of Li_2S decomposition reaction on (c) NC and (d) TiSA-NC. Adsorption energy of (e) NC and (f) TiSA-NC for Li_2S, respectively. Side view for charge density difference of Li_2S adsorption on (g) NC and (h) TiSA-NC. The yellow and blue sections represent the electron accumulate and lose region, respectively. The iso-surface is set to 0.004 e·Bohr^{-3}. (i) Calculated TDOS of TiSA-NC and NC.

1.9800 eV. This was in accordance with the charging test results in Figs. 4(a), 4(c) and 4(d). The anchoring ability of Li_2S toward a target material could be reflected by the E_{ads} [42]. As shown in Figs. 5(e) and 5(f), the Li_2S had stronger E_{ads} on TiSA-NC (−4.06 eV) than that on NC (−3.06 eV), which guaranteed the former had stronger immobilizing ability toward Li_2S thus suppressing the shuttle effect. The charge density differences exhibited the electron transfer between the substrates and Li_2S. For the TiSA-NC (Fig. 5(h)), there was more electron transfer between Ti and S compared with NC (Fig. 5(g)), which meant the weakening of Li-S bond and therefore the reducing of the decomposition barriers of Li_2S [22]. The conductivity of the substrate also had a great influence on the reversible conversion of the LiPSs [43, 44]. We calculated the total DOS (TDOS) of NC and TiSA-NC. As shown in Fig. 5(i), it could be seen that the density of states at the Fermi level of the substrate was increased after the introduction of TiSAs, which was consistent with the results of EIS test and further proved that the incorporation of TiSAs could accelerate the electron transportation favorable for the LiPSs fast conversion.

Integrating the experimental data with DFT calculation results, we can get a glimpse into the influence mechanism of the TiSAs on the LiPSs conversion kinetics, as shown in Fig. 6. The Ti-N_4 active sites adjusted the charge distribution on NC which increased the E_{ads} towards LiPSs and thus the weakened Li-S bond lowered the conversion reaction barrier of the rate-limiting step of the LiPSs. In addition, Ti-N_4 active sites increased TDOS near the Fermi level, which was facile for improving electronic conductivity of the NC texture. The lowered reaction barrier and fast electron transportation were beneficial to boost the LiPSs conversion kinetics. Consequently, the Li-S batteries based on TiSA-NC exhibited electrochemical performance prior to that based on NC.

4 Conclusions

In summary, the mesoporous single Ti atom-incorporated carbonaceous material, TiSA-NC had been prepared by the pyrolysis of Ti-ZIF-8, which was synthesized by similar approach for the conventional ZIF-8 except for an addition of a small amount of titanium acetyl acetone in the zinc nitrate solution. Attributed to the large specific surface area and affluent porous structure which were inherited from Ti-ZIF-8, the TiSA-NC could provide sufficient reaction interface with abundant active sites and shortened transport paths for electrons and lithium ions. Furthermore, the incorporation of TiSAs onto NC textures optimized their electronic structural coefficients including the adjusted charge distribution between the constituent atoms and the improved TDOS near the Fermi level. The optimized charge distribution strengthened the polarity and hence enhanced the E_{ads} toward LiPSs, which consequently not only declined the reaction barrier in their rate-limiting conversion step but also inhabited the shuttle effect of the sulfur species; while the increased TDOS near the Fermi level is beneficial to the electronic conductivity improvement of the NC textures, as verified by the experimental observations and theoretical calculation results. These merits enabled fast reversible conversion of the LiPSs. Therefore, the Li-S batteries based on TiSA-NC could deliver impressive electrochemical properties, including a large reversible capacity of

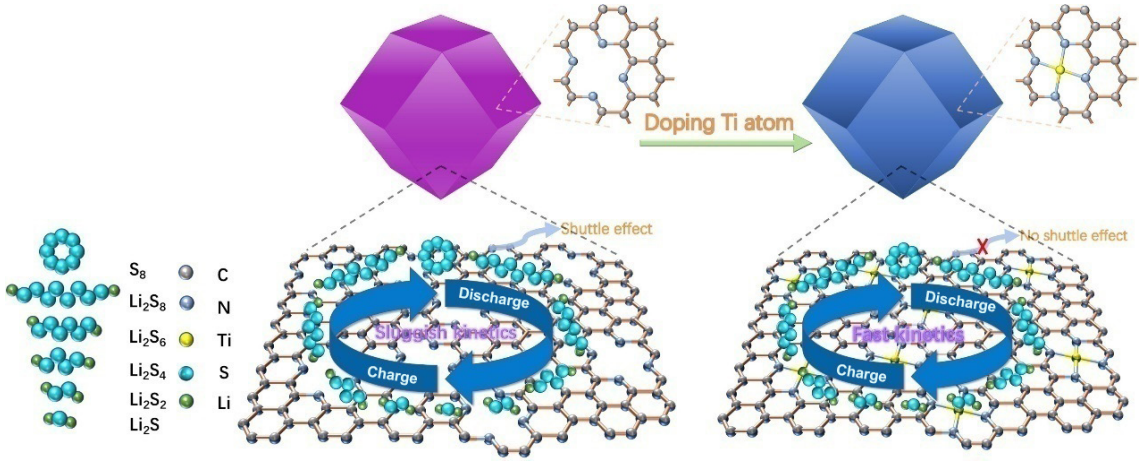

Figure 6 Schematic illustration of the effect of TiSA-NC in improving the conversion kinetics.

1077 mAh·g^{-1} at 0.1 C, a high-rate capacity of 541 mAh·g^{-1} at 3 C and a superior long-term stability with a capacity fading rate of 0.053% per cycle for 500 cycles at 0.5 C. This study may open a new avenue to design and construct single atom catalysts and provide a solution for the practical application of high performance Li-S batteries.

Electronic Supplementary Material: Supplementary material (SEM measurements, EIS, TGA, XRD, XPS curves, and Table S1) is available in the online version of this article at https://doi.org/10.26599/NR.2025.94907114.

Data availability

All data needed to support the conclusions in the paper are presented in the manuscript and the Electronic Supplementary Material. Additional data related to this paper may be requested from the corresponding author upon request.

Acknowledgements

This work was financially supported by the National Natural Science Foundation of China (Nos. 12175098 and 11727902) and this research was supported by Jiangxi Provincial Innovation Talents of Science and Technology (No. 20165BCB18003).

Declaration of competing interest

The authors report no declarations of interest.

Author contribution statement

J. F. H.: Conceptualization, methodology, writing – original draft. Y. F. X.: Data curation, software. Z. G. H.: Data curation, software. G. H. H.: Visualization, investigation, writing – review & editing. Z. H. Z.: Data curation, software, validation. F. P. X.: Conceptualization, methodology, writing – original draft. L. W.: Investigation. L. Z.: Software, validation. Y. Z.: Conceptualization, methodology, writing – original draft, supervision. All the authors have approved the final manuscript.

Use of AI statement

None.

References

[1] Bruce, P. G.; Freunberger, S. A.; Hardwick, L. J.; Tarascon, J. M. Li–O_2 and Li–S batteries with high energy storage. *Nat. Mater.* **2012**, *11*, 19–29.

[2] Li, Y. J.; Guo, S. J. Material design and structure optimization for rechargeable lithium-sulfur batteries. *Matter* **2021**, *4*, 1142–1188.

[3] Pang, Q.; Liang, X.; Kwok, C. Y.; Nazar, L. F. Advances in lithium-sulfur batteries based on multifunctional cathodes and electrolytes. *Nat. Energy* **2016**, *1*, 16132.

[4] Manthiram, A.; Fu, Y. Z.; Chung, S. H.; Zu, C. X.; Su, Y. S. Rechargeable lithium-sulfur batteries. *Chem. Rev.* **2014**, *114*, 11751–11787.

[5] Kim, H.; Bang, S.; Min, K. J.; Ham, Y. G.; Park, S. J.; Sun, Y. K. Achieving high-performance Li–S batteries via polysulfide adjoining interface engineering. *ACS Appl. Mater. Interfaces* **2021**, *13*, 39435–39445.

[6] Seo, H. K.; Hwa, Y.; Chang, J. H.; Park, J. Y.; Lee, J. S.; Park, J.; Cairns, E. J.; Yuk, J. M. Direct visualization of lithium polysulfides and their suppression in liquid electrolyte. *Nano Lett.* **2020**, *20*, 2080–2086.

[7] Luo, S. R.; Wu, F. X.; Yushin, G. Strategies for fabrication, confinement and performance boost of Li_2S in lithium-sulfur, silicon-sulfur & related batteries. *Mater. Today* **2021**, *49*, 253–270.

[8] Chen, F.; Ma, L. L.; Ren, J. G.; Luo, X. Y.; Liu, B. B.; Zhou, X. Y. Sandwich-type nitrogen and sulfur codoped graphene-backboned porous carbon coated separator for high performance lithium-sulfur batteries. *Nanomaterials* **2018**, *8*, 191.

[9] Guo, W.; Fu, Y. Z. A Perspective on energy densities of rechargeable Li-S batteries and alternative sulfur-based cathode materials. *Energy Environ. Mater.* **2018**, *1*, 20–27.

[10] Liu, X.; Huang, J. Q.; Zhang, Q.; Mai, L. Q. Nanostructured metal oxides and sulfides for lithium-sulfur batteries. *Adv. Mater.* **2017**, *29*, 1601759.

[11] Pang, Q.; Kwok, C. Y.; Kundu, D.; Liang, X.; Nazar, L. F. Lightweight metallic MgB_2 mediates polysulfide redox and promises high-energy-density lithium-sulfur batteries. *Joule* **2019**, *3*, 136–148.

[12] Ji, X. L.; Lee, K. T.; Nazar, L. F. A highly ordered nanostructured carbon-sulphur cathode for lithium-sulphur batteries. *Nat. Mater.* **2009**, *8*, 500–506.

[13] Seh, Z. W.; Sun, Y. M.; Zhang, Q. F.; Cui, Y. Designing high-energy lithium-sulfur batteries. *Chem. Soc. Rev.* **2016**, *45*, 5605–5634.

[14] Seh, W. Z.; Li, W. Y.; Cha, J. J.; Zheng, G. Y.; Yang, Y.; McDowell, M. T.; Hsu, P. C.; Cui, Y. Sulphur-TiO_2 yolk–shell nanoarchitecture with internal void space for long-cycle lithium-sulphur batteries. *Nat. Commun.* **2013**, *4*, 1331.

[15] Wang, Y. K.; Zhang, R. F.; Chen, J.; Wu, H.; Lu, S. Y.; Wang, K.; Li, H. L.; Harris, C. J.; Xi, K.; Kumar, R. V. et al. Enhancing catalytic

activity of titanium oxide in lithium-sulfur batteries by band engineering. *Adv. Energy Mater.* **2019**, *9*, 1900953.
[16] Li, Z.; Zhang, J. T.; Guan, B. Y.; Wang, D.; Liu, L. M.; Lou, X. W. A sulfur host based on titanium monoxide@carbon hollow spheres for advanced lithium-sulfur batteries. *Nat. Commun.* **2016**, *7*, 13065.
[17] Qiao, B. T.; Wang, A. Q.; Yang, X. F.; Allard, L. F.; Jiang, Z.; Cui, Y. T.; Liu, J. Y.; Li, J.; Zhang, T. Single-atom catalysis of CO oxidation using Pt_1/FeO_x. *Nat. Chem.* **2011**, *3*, 634–641.
[18] Xie, J.; Li, B. Q.; Peng, H. J.; Song, Y. W.; Zhao, M.; Chen, X.; Zhang, Q.; Huang, J. Q. Implanting atomic cobalt within mesoporous carbon toward highly stable lithium-sulfur batteries. *Adv. Mater.* **2019**, *31*, 1903813.
[19] Wang, C. G.; Song, H. W.; Yu, C. C.; Ullah, Z.; Guan, Z. X.; Chu, R. R.; Zhang, Y. F.; Zhao, L. Y.; Li, Q.; Liu, L. W. Iron single-atom catalyst anchored on nitrogen-rich MOF-derived carbon nanocage to accelerate polysulfide redox conversion for lithium sulfur batteries. *J. Mater. Chem. A* **2020**, *8*, 3421–3430.
[20] Wu, J. L.; Chen, J. M.; Huang, Y.; Feng, K.; Deng, J.; Huang, W.; Wu, Y. L.; Zhong, J.; Li, Y. G. Cobalt atoms dispersed on hierarchical carbon nitride support as the cathode electrocatalyst for high-performance lithium-polysulfide batteries. *Sci. Bull.* **2019**, *64*, 1875–1880.
[21] Zhang, L. L.; Liu, D. B.; Muhammad, Z.; Wan, F.; Xie, W.; Wang, Y. J.; Song, L.; Niu, Z. Q.; Chen, J. Single nickel atoms on nitrogen-doped graphene enabling enhanced kinetics of lithium-sulfur batteries. *Adv. Mater.* **2019**, *31*, 1903955.
[22] Zhou, G. M.; Zhao, S. Y.; Wang, T. S.; Yang, S. Z.; Johannessen, B.; Chen, H.; Liu, C. W.; Ye, Y. S.; Wu, Y. C.; Peng, Y. et al. Theoretical calculation guided design of single-atom catalysts toward fast kinetic and long-life Li–S batteries. *Nano Lett.* **2020**, *20*, 1252–1261.
[23] Han, Z. Y.; Zhao, S. Y.; Xiao, J. W.; Zhong, X. W.; Sheng, J. Z.; Lv, W.; Zhang, Q. F.; Zhou, G. M.; Cheng, H. M. Engineering d–p orbital hybridization in single-atom metal-embedded three-dimensional electrodes for Li-S batteries. *Adv. Mater.* **2021**, *33*, 2105947.
[24] Cao, F. L.; Zhang, X. K.; Jin, Z. H.; Zhang, J. Y.; Tian, Z. Y.; Kong, D. B.; Li, Y. P.; Li, Y. T.; Zhi, L. J. Electronegativity matching of asymmetrically coordinated single-atom catalysts for high-performance lithium-sulfur batteries. *Adv. Energy Mater.* **2024**, *14*, 2303893.
[25] Wang, A. Q.; Li, J.; Zhang, T. Heterogeneous single-atom catalysis. *Nat. Rev. Chem.* **2018**, *2*, 65–81.
[26] Bai, J. R.; Fu, Y.; Zhou, P.; Xu, P.; Wang, L. L.; Zhang, J. P.; Jiang, X. K.; Zhou, Q. F.; Deng, Y. Y. Synergies of atomically dispersed Mn/Fe single atoms and Fe nanoparticles on N-doped carbon toward high-activity eletrocatalysis for oxygen reduction. *ACS Appl. Mater. Interfaces* **2022**, *14*, 29986–29992.
[27] Chang, F. F.; Zhu, K.; Liu, C. H.; Wei, J. C.; Yang, S. W.; Zhang, Q.; Yang, L.; Wang, X. L.; Bai, Z. Y. Construction of Cu–Ni atomic pair with bimetallic atom-cluster sites for enhanced CO_2 electroreduction. *Adv. Funct. Mater.* **2024**, *34*, 2400893.
[28] Kresse, G.; Furthmüller, J. Efficient iterative schemes for *ab initio* total-energy calculations using a plane-wave basis set. *Phys. Rev. B* **1996**, *54*, 11169–11186.
[29] Ernzerhof, M.; Scuseria, G. E. Assessment of the Perdew–Burke–Ernzerhof exchange-correlation functional. *J. Chem. Phys.* **1999**, *110*, 5029–5036.
[30] Perdew, J. P.; Burke, K.; Ernzerhof, M. Generalized gradient approximation made simple [Phys. Rev. Lett. 77, 3865 (1996)]. *Phys. Rev. Lett.* **1997**, *78*, 1396.
[31] Grimme, S.; Antony, J.; Ehrlich, S.; Krieg, H. A consistent and accurate *ab initio* parametrization of density functional dispersion correction (DFT-D) for the 94 elements H–Pu. *J. Chem. Phys.* **2010**, *132*, 154104.
[32] Momma, K.; Izumi, F. *VESTA 3* for three-dimensional visualization of crystal, volumetric and morphology data. *J. Appl. Cryst.* **2011**, *44*, 1272–1276.
[33] Wang, V.; Xu, N.; Liu, J. C.; Tang, G.; Geng, W. T. VASPKIT: A user-friendly interface facilitating high-throughput computing and analysis using VASP code. *Comput. Phys. Commun.* **2021**, *267*, 108033.
[34] Henkelman, G.; Uberuaga, B. P.; Jónsson, H. A climbing image nudged elastic band method for finding saddle points and minimum energy paths. *J. Chem. Phys.* **2000**, *113*, 9901–9904.
[35] Ma, R. Z.; Li, Q. H.; Yan, J.; Tao, Y.; Hu, S. Y.; Liu, D. H.; Gong, J. X.; Xiong, Y. Thermodynamically controllable synthesis of ZIF-8 exposing different facets and their applications in single atom catalytic oxygen reduction reactions. *Nano Res.* **2023**, *16*, 9618–9624.
[36] Zhu, J.; Wang, X. Y.; Ke, T.; Jia, M. J.; Jin, B. Y.; Li, Y. Y.; Yang, Q. W.; Ren, L. H.; Ren, Y. Y.; Cheng, D. G. et al. Nickel single atom overcoordinated active sites to accelerate the electrochemical reaction kinetics for Li-S cathode. *J. Energy Chem.* **2023**, *78*, 203–210.
[37] Xu, Z. L.; Zhang, S. L.; Liu, J. Y.; Xiao, Z. H.; Yang, M.; Tang, A. D. Kaolinite nanoscroll significantly inhibiting polysulfide ions shuttle in lithium sulfur batteries. *Appl. Clay Sci.* **2022**, *224*, 106516.
[38] Qi, C.; Zu, S.; Zhu, X. K.; Zhang, T.; Li, L. Y.; Song, L.; Jin, Y. C.; Zhang, M. D. Bamboo-shaped Co@NCNTs as superior sulfur host for Li-S batteries. *Appl. Surf. Sci.* **2022**, *601*, 154245.
[39] Xiao, T. J.; Yang, Y. M.; Yang, M. Z.; Liu, W. L.; Li, M.; Ren, M. M.; Cai, F. P.; Wang, Y. H. CoOOH-hierarchical porous carbon-sulfur as an excellent cathode for Li-S batteries. *J. Alloys Compd.* **2022**, *923*, 166334.
[40] Tian, Y. H.; Yang, Z. Y.; Wang, H.; Xiong, W. L.; Lin, X. L.; Wang, S. J.; Kong, F. G.; Li, P.; Xi, Y. B.; Zhang, F. S. et al. Nitrogen-doped 3D carbon hybrids based on modified lignin as sulfur host for high-performance lithium-sulfur batteries. *J. Power Sources* **2024**, *621*, 235322.
[41] Liu, C.; Wu, P. F.; Chen, X. Z.; Gu, C.; Chen, S. H.; Mei, X.; Liu, A. H. Synergy of physical and chemical constraints for stable lithium-sulfur batteries. *J. Alloys Compd.* **2022**, *927*, 167038.
[42] Tao, X. Y.; Wang, J. G.; Liu, C.; Wang, H. T.; Yao, H. B.; Zheng, G. Y.; Seh, Z. W.; Cai, Q. X.; Li, W. Y.; Zhou, G. M. et al. Balancing surface adsorption and diffusion of lithium-polysulfides on nonconductive oxides for lithium-sulfur battery design. *Nat. Commun.* **2016**, *7*, 11203.
[43] Tian, S. H.; Zeng, Q.; Liu, G.; Huang, J. J.; Sun, X.; Wang, D.; Yang, H. C.; Liu, Z.; Mo, X. C.; Wang, Z. X. et al. Multi-dimensional composite frame as bifunctional catalytic medium for ultra-fast charging lithium-sulfur battery. *Nanomicro Lett.* **2022**, *14*, 196.
[44] Wang, R. R.; Wu, R. B.; Yan, X. X.; Liu, D.; Guo, P. F.; Li, W.; Pan, H. G. Implanting single Zn atoms coupled with metallic Co nanoparticles into porous carbon nanosheets grafted with carbon nanotubes for high-performance lithium-sulfur batteries. *Adv. Funct. Mater.* **2022**, *32*, 2200424.